Research Square

Preprints are preliminary reports that have not undergone peer review.
They should not be considered conclusive, used to inform clinical practice,
or referenced by the media as validated information.

Architectured AlN/Al Composites Produced by Material Extrusion and Pressure Infiltration: Processing–Structure–Property Relationships

Štefan Nagy
nagy.stefan@savba.sk
Institute of Materials and Machine Mechanics of the Slovak Academy of Sciences
Lilla Vály
RHP Technology (Austria)
Mária Vozárová
RHP Technology (Austria)
Erich Neubauer
RHP Technology (Austria)
Andrej Opálek
RHP Technology (Austria)
Lukáš Karaffa
Institute of Materials and Machine Mechanics of the Slovak Academy of Sciences
Veronika Nagy Trembošová
Institute of Materials and Machine Mechanics of the Slovak Academy of Sciences
Selim Burak Cantürk
Institute of Materials and Machine Mechanics of the Slovak Academy of Sciences
Peter Oslanec
Institute of Materials and Machine Mechanics of the Slovak Academy of Sciences

Research Article

Keywords: material extrusion, Fused Granulate Fabrication, AlN–Al composite, debinding, sintering, metal infiltration

Posted Date: July 30th, 2026

DOI: https://doi.org/10.21203/rs.3.rs-10194839/v1

License: This work is licensed under a Creative Commons Attribution 4.0 International License. Read Full License

Additional Declarations: No competing interests reported.

Abstract

This work presents a hybrid manufacturing route combining material extrusion of porous AlN preforms with pressure-assisted aluminum infiltration for the fabrication of architectured AlN/Al composites. Porous AlN preforms were produced by Material Extrusion (MEX) Fused Granulate Fabrication (FGF), followed by debinding and sintering to obtain an interconnected ceramic framework. The porous AlN line infill structures were subsequently infiltrated with molten aluminum alloy under pressure, resulting in a dense interpenetrating ceramic–metal composite. Physical parameters and the microstructural evolution throughout the processing route was investigated using scanning electron microscopy (SEM), energy-dispersive spectroscopy (EDS), and X-ray computed tomography (XCT). Microstructural observations confirmed homogeneous aluminum distribution and a well-defined AlN/Al interface throughout the composite. Tomographic analysis revealing a final composite containing 75.4 vol.% AlN and 24.6 vol.% Al. The overall porosity determined by X-ray tomography and microstructural analysis was approximately 0.68 vol.%. Thermomechanical characterization showed stable behavior up to 500°C, with coefficients of thermal expansion ranging from 11.6 to 12.9 × 10^{-6} K^{-1} after thermal stabilization. Compression testing revealed moderate anisotropy associated with the printed architecture, with average compressive strengths of 511 MPa and 567 MPa in the XY and Z directions, respectively.

1. Introduction

The integration of additive manufacturing with liquid metal infiltration introduces innovative fabrication strategies for ceramic–metal or metal–metal composites, enabling precise control over the macrostructure of the final composite. Such control directly influences the physical properties of the material and allows extensive tailoring of mechanical and thermophysical behavior. In recent years, additive manufacturing of porous preforms followed by liquid metal infiltration has emerged as an effective route for producing interpenetrating composite architectures that are difficult to achieve using conventional processing techniques [1, 2, 3, 4, 5]. Material extrusion (MEX) technologies—such as filament-based fused deposition modeling (FDM), pellet-based extrusion, and direct ink writing (DIW)—are cost-effective additive manufacturing routes capable of fabricating complex geometries. Highly filled polymers or inks containing ceramic or metallic particles have therefore become a focal point of research across multiple scientific disciplines [6, 7, 8, 9]. After printing, debinding and sintering steps are employed to obtain open porous ceramic and metallic structures suitable for subsequent infiltration. Among the various material systems compatible with these technologies, aluminum nitride (AlN)–reinforced aluminum (Al) composites are emerging as advanced multifunctional materials that combine the advantageous properties of both constituents [10, 11, 12].

Aluminum nitride is characterized by high thermal conductivity, electrical insulation, low coefficient of thermal expansion, and excellent thermal stability, while aluminum offers low density, good ductility, high specific strength, and corrosion resistance [13, 14]. The combination of AlN and Al in a composite architecture is therefore particularly attractive for aerospace, automotive, and electronic packaging applications, where simultaneous thermal management and mechanical performance are required [15, 16, 17, 18, 19]. Despite this potential, studies focusing specifically on AlN–Al composites fabricated via additive manufacturing routes remain limited, especially in comparison to more extensively investigated oxide- or carbide-based systems [1, 2, 20, 21].

Previous research has demonstrated the feasibility of producing porous ceramic or metallic scaffolds by additive manufacturing followed by metal infiltration. Zhu et al. [22] reported an Al/Al_2O_3 aluminum matrix composite fabricated using stereolithography (SLA) 3D printing combined with squeeze casting, achieving a 112.4% increase in strength and a 54.8% improvement in elastic modulus compared to pure aluminum. Meng et al. [23] investigated Al_2O_3 scaffolds produced by direct ink writing and subsequently infiltrated with aluminum, revealing pronounced

anisotropic mechanical behavior governed by layer orientation and zigzag printing patterns, which enabled tunable flexural and compressive properties. Pressureless infiltration of molten metals into AlN ceramic preforms has been previously demonstrated for magnesium-based matrix systems, resulting in improved mechanical and thermophysical properties [24]. More recently, laser-based additive manufacturing approaches have been used to fabricate Al–AlN architectures directly; however, such methods often involve high processing costs and limited scalability [6]. In contrast, extrusion-based additive manufacturing of AlN ceramic preforms followed by aluminum infiltration offers a flexible, scalable, and cost-effective alternative for producing complex AlN–Al composite structures.

The novelty of the present work lies in combining pellet-based material extrusion of AlN preforms with pressure-assisted aluminum infiltration and in the systematic investigation of the resulting composite. Particular emphasis is placed on the microstructural evolution throughout all processing stages and on the thermomechanical properties of the final composite. The insights gained from this work contribute to the development of advanced AlN–Al composites with tailored architectures.

2. Experimental

The preparation route of the AlN–Al composite is schematically illustrated in Fig. 1. Porous ceramic preforms were fabricated from granulated aluminum nitride (AlN) feedstock using material extrusion. Subsequently, an aluminum alloy containing 1.3 wt.% Mg was prepared for pressure infiltration to enhance the wettability of the AlN framework. Before infiltration, the alloy was melted and homogenized in an autoclave furnace.

The AlN porous preforms were fabricated using an EXAM II extrusion-based 3D printing system (AIM3D GmbH). A cylindrical model with dimensions of 20 mm × 7 mm was designed and sliced using CURA software. The slicing strategy employed a 70% line infill pattern, without perimeters and without top or bottom solid layers, in order to obtain an open porous structure suitable for metal infiltration. The main printing parameters were as follows: nozzle diameter 0.4 mm, nozzle temperature 150°C, and build platform temperature 60°C. The printing orientation was defined using a Cartesian coordinate system. The X and Y directions correspond to the printing plane, while the Z direction represents the build direction, perpendicular to the deposited layers.

After printing, a two-step debinding process was applied. First, wet debinding was performed to dissolve approximately 5 wt% of the binder by immersing the printed parts in isopropanol at 72°C for 48 h. The samples were then dried in air. Subsequently, thermal debinding was carried out in an argon atmosphere up to 500°C in order to remove the remaining organic binder components. Following debinding, the samples were sintered in a nitrogen (N_2) atmosphere at a temperature of 1650°C to consolidate the AlN ceramic framework.

For the infiltration process, the porous preforms were secured using molybdenum wires and attached to a graphite immersion holder. The aluminum alloy was melted under an argon atmosphere, and the porous preforms were immersed in the aluminum melt at the adjusted infiltration temperature. Subsequently, the infiltration pressure was applied. The infiltration parameters were as follows: temperature 750°C, infiltration time 5 min, and pressure 3 MPa. During cooling, the infiltrated samples were lifted out of the melt under the applied pressure and released after the temperature decreased below the melting point of aluminum.

The microstructure analysis was performed with a Jeol JSM 6610 SEM equipped with SEI and BS detectors. Oxford Instruments X-max (50 mm2) EDX detector was used for chemical analysis. The cross section samples were prepared using standard metallography preparation: cutting, grinding (sand papers with 22 and 15 um grain size),

polishing (polishing suspension with 9,6,3,1 um grain size). Micro-porosity was calculated from back scattered micrographs using Image J software.

X-ray computed tomography (XCT) analysis was performed using an industrial CT system Nikon XT H 225ST equipped with a reflection-type X-ray source and a tungsten target. The scanning was conducted at an acceleration voltage of 210 kV and a power of 6.3 W, without the use of beam filtration. A total of 720 projections were acquired, with four frames averaged per projection and an exposure time of 1 s per frame. The effective pixel size was 25 µm. The reconstruction of volumetric data was carried out using XTEK CT PRO 3D, with beam hardening and noise reduction corrections applied to improve image quality and reduce common CT artefacts. Subsequent data processing and analysis were performed in VGStudio Max.

The thermal expansion behavior and dimensional stability of the fabricated AlN/Al composites were characterized using a Linseis L75 vertical dilatometer. The measurements were performed in a pure argon atmosphere to prevent oxidation. The samples were placed in a high-purity quartz (silica) sample holder. Size of the samples were 4mm x 4mm x 6mm. A total of three consecutive heating and cooling cycles were conducted for each specimen to evaluate the reproducibility and thermal stabilization of the material. The temperature range was set from room temperature to 500°C, with a constant heating and cooling rate of 3°C/min. The initial sample length (L_0) was recorded for each measurement to calculate the relative elongation ($\Delta L/L_0$). The experimental data were processed and evaluated using the Linseis TA Software package, where the instantaneous coefficient of thermal expansion (CTE) was determined from the heating curves.

The compressive mechanical properties of the AlN/Al composites were evaluated at room temperature using a Zwick/Roell Z100 universal testing machine. Cylindrical specimens with a nominal diameter (d) of approximately 4 mm and a length (L) of 8.4 mm were prepared for testing. The determination of the compression modulus was performed at a loading rate of 9 MPa/s. To capture the deformation behavior accurately, the speed until the crush yield point was set at a strain rate of 0.00025 s^{-1}, while the subsequent test speed was maintained at a constant strain rate of 0.002 s^{-1}. The compressive strength (σ_{dM}) and the 0.2% offset yield strength ($\sigma_{d0.2}$) were recorded for each specimen. Average strength values were calculated from 4 samples for each printing directions X(Y) and Z.

3. Results

For the infiltration of porous AlN material 4 samples were 3D printed. The weight loss and size shrinkage results after debinding and sintering are summarised in table 1. After liquid debinding the samples on average lost 5% of weight and after thermal debinding additional 10%. After the debinding process the samples were carefully moved to the sintering furnace. Sintering at 1650°C resulted in minimal weight loss indicating that the thermal debinding removed most of the binding agents in the structure.

Table 1
, Physical parameters of AlN preforms across processing stages

Sample	As- printed			Weight after Solvent Debinding (g)	Weight after Thermal Debinding (g)	Sintered			Overall weight loss (%)
	Weight (g)	Height (mm)	Diameter (mm)			Weight (g)	Height (mm)	Diameter (mm)	
FDM1912	3.72	6,83	20,5	3.55	3.18	3.17	6,6	19,5	14.78
FDM1913	3.88	6,85	20,8	3.68	3.29	3.28	6,6	19,3	15.46
FDM1914	3.75	6,84	20,6	3.59	3.19	3.17	6,6	19,4	15.47
FDM1915	3.79	6,81	20,7	3.61	3.23	3.23	6,5	19,3	14.78

The quality and surface morphology of the as-printed and sintered samples were examined in detail using electron microscopy, as shown in Fig. 2. The macrostructure clearly reveals the line infill structure of the 3D-printed sample, which remains consistent after the sintering process. The surface microstructure (Fig. 2b) of the as-printed sample shows AlN particles homogeneously embedded in the binder system. Furthermore, Fig. 2c provides a more detailed view of the binder structure in a fractured area at the edge of the sample. After sintering, the gray color of the as-printed sample (Fig. 2a) changed to white color (Fig. 2e), indicating the removal of organic binders. Examination of the sample surface (Fig. 2g) revealed the morphology and structure of the sintered AlN particles. Larger particles are also visible on the surface (Fig. 2h), indicating a higher oxygen content as measured by EDS.

The final composite structure after Al-1.3 wt.% Mg melt infiltration is summarized in Fig. 3. The prepared sample shown in Fig. 3a, after the infiltration process, was cleaned of residual Al melt and cut for SEM, dilatometric, and compression test analyses. Macroscale cross-sections (Figs. 3a–3b) reveal a macroscopically defect-free, fully dense structure across the predefined X, Y, and Z build axes. Micrographs viewed from the printing plane perspective (Figs. 3c–3d) demonstrate that the liquid metal completely occupied the primary channels left by the 70% line infill pattern, successfully wrapping around the oval-shaped AlN struts. Interconnection of several AlN line components is shown on Fig. 3d. Figure 3e, together with EDS analysis, represents a section in the Z-direction perspective, showing a distinct elemental separation of Al, N, and Mg on the interface.

A detailed investigation of the AlN ceramic microstructure and the AlN/Al interface is presented in Fig. 4. A well-defined AlN/Al interface can be observed in Figs. 4a and 4d. The ceramic regions contain high-contrast particles and exhibit isolated microporosity, while microporosity is also present within the aluminum matrix. Higher-magnification imaging of the ceramic phase (Fig. 4b) reveals the detailed microstructure of the sintered AlN, including isolated pores resulting from incomplete local densification. The microporosity of the aluminum alloy and the ceramic component, determined from SEM micrographs, was 0.47% and 0.63%, respectively. Figure 4c shows the interface between two adjacent 3D-printed AlN lines, demonstrating a homogeneous bond between the deposited layers. EDS analysis of the interfacial region shown in Fig. 4d revealed clearly separated distributions of aluminum and nitrogen, indicating limited interfacial reactions during infiltration. High-contrast particles observed in the ceramic phase by SEM are attributed to yttrium-rich oxide phases. Higher-magnification imaging of the interface (Fig. 4e), supported by EDS analysis, revealed larger yttrium-rich oxide clusters. These features are consistent with the surface particles previously observed on the AlN preforms after sintering (Fig. 2h).

To resolve the spatial distribution of the constituent phases and evaluate the infiltration quality, X-ray micro-computed tomography was performed over an analyzed volume of 38.18 mm^3 (Fig. 5). Phase segmentation revealed a volumetric composition of 75.4 vol.% AlN and 24.6 vol.% Al, confirming successful infiltration of the additively

manufactured ceramic framework. The computed residual macroporosity within the aluminum phase was limited to 0.36%, indicating the absence of significant infiltration defects or large structural voids. Owing to the voxel resolution of 25 µm, X-ray tomography is sensitive only to macroscopic pores, whereas finer microporosity remains below its detection limit. No macroporosity was detected within the AlN ceramic phase by X-ray micro-computed tomography, indicating that the ceramic framework was free of macroscopic defects above the 25 µm detection limit. By combining the CT and SEM analyses, the overall porosity of the composite was estimated to be approximately 0.68 vol.%.

The thermomechanical response of the interpenetrating composites over three consecutive thermal cycles from 100°C to 500°C is plotted in Fig. 6. The relative elongation results (Fig. 6a) indicate a small distinction between the printing plane (XY) and the build direction (Z). In the XY plane, the composite demonstrates high dimensional stability and reversibility across all cycles. However, the Z-axis exhibits a notable phenomenon during the first cycle: a residual shrinkage of approximately 0.22% was measured upon cooling to room temperature. In the subsequent second and third cycles, the Z-axis expansion became reproducible and stabilized. The instantaneous CTE values, evaluated from 100°C to 500°C (Fig. 5b), further support these findings. In the first cycle, the Z-axis CTE shows a decreasing trend, starting from higher values and stabilizing at a lower plateau (approx. 7.3–11.4 × 10^{-6} K^{-1}). This behavior is characteristic of internal stress relief. From the second cycle onwards, the CTE profiles for both directions become stable and consistent, with mean values ranging between 11.6 and 12.9 × 10^{-6} K^{-1}.

Uniaxial compression testing confirmed that the macroscale directional printing path dictates the final mechanical breakdown behavior. The composite exhibits moderate mechanical anisotropy, developing an average compressive strength of 511 MPa parallel to the horizontal printing plane (XY direction), compared to 567 MPa parallel to the vertical build direction (Z direction). This variation highlights how the stacked, interconnected 2D line-infill struts redistribute mechanical loads differently depending on the orientation of the applied stress vector relative to the internal ceramic framework layers.

Table 2
Compression test measurement

Sample	Compressive strength (MPa)				Average compressive strength (MPa)
	Test 1	Test 2	Test 3	Test 4	
AlN/Al_XY	539	466	515	523	**511**
AlN/Al_Z	594	494	592	588	**567**

4. Discussion

The present study demonstrates that extrusion-based additive manufacturing combined with liquid metal infiltration is an effective route for producing architectured AlN/Al composites with controlled internal geometry and low residual porosity. Unlike conventional composite processing methods, the material extrusion approach enables direct control of the pore architecture prior to infiltration, allowing the final composite structure to be designed at the printing stage. The preservation of the line-infill architecture throughout debinding, sintering, and infiltration highlights the suitability of the selected processing route for manufacturing complex ceramic–metal composites.

The structural integrity of the printed AlN preforms is a key factor governing the success of the subsequent infiltration process. The relatively small and uniform shrinkage observed after sintering indicates homogeneous densification of the ceramic framework while maintaining the interconnected pore network generated by the 70% line-infill strategy.

Similar observations have been reported for additively manufactured ceramic preforms used for metal infiltration, where preservation of pore connectivity is essential for achieving complete metal penetration and minimizing residual defects [1,22–24]. The selected 70% line infill represented a compromise between maintaining sufficient interconnected porosity for complete infiltration and ensuring structural integrity and dimensional stability throughout all processing stages.

Microstructural characterization confirmed that the printed architecture directly influenced infiltration efficiency. The interconnected channels created during the material extrusion process enabled effective penetration of the Al–1.3 wt.% Mg alloy throughout the ceramic framework. No large uninfiltrated regions or macroscopic defects were observed in the investigated cross-sections. Furthermore, X-ray tomography revealed a residual macroporosity of only 0.36%, demonstrating that the designed pore architecture provided favorable pathways for molten metal flow. The resulting phase fractions of 75.4 vol.% AlN and 24.6 vol.% Al indicate the successful formation of a ceramic-rich interpenetrating composite structure. These results demonstrate that the architecture generated by additive manufacturing not only defines the final geometry but also governs infiltration quality and the resulting composite density. Furthermore, SEM micrographs revealed microporosities of 0.47% and 0.63% in the aluminum alloy and AlN ceramic phases, respectively. Taking the phase fractions into account, the overall porosity of the composite was calculated to be approximately 0.68 vol.%. At the microscale, SEM and EDS analyses revealed a distinct AlN/Al interface with clearly separated elemental distributions of aluminum and nitrogen, indicating limited interfacial reactions during infiltration at 750°C. High-magnification observations further revealed isolated microporosity within the ceramic struts and yttrium-rich oxide particles distributed throughout the AlN phase. These particles originate from the Y_2O_3 sintering additive present in the commercial AlN feedstock and are associated with the liquid-phase sintering mechanism commonly employed for densification of AlN ceramics. The absence of extensive reaction products at the ceramic–metal interface suggests that the selected infiltration conditions were sufficient to ensure bonding without promoting excessive interfacial reactions that could deteriorate composite performance. The yttrium-rich oxide particles observed at the AlN/Al interface originated during the sintering of the AlN ceramic and were also identified on the surface of the porous preforms by SEM analysis.

The influence of the additively manufactured architecture becomes particularly evident in the thermomechanical behavior of the composite. Following thermal stabilization, the coefficient of thermal expansion ranged from 11.6 to $12.9 \times 10^{-6}\ K^{-1}$, significantly lower than that of pure aluminum and consistent with previously reported AlN-reinforced aluminum composites [17, 18]. However, the most notable feature was the anisotropic response observed between the printing plane and build direction. The residual shrinkage of approximately 0.22% measured in the Z direction during the first thermal cycle suggests the presence of residual stresses generated during infiltration and solidification within the layered architecture. The first heating cycle effectively acted as a stress-relief treatment, resulting in stable elongation and CTE behavior during subsequent cycles.

The anisotropic thermal expansion behavior can be directly linked to the layer-by-layer deposition strategy. In the XY plane, the aluminum matrix can expand relatively freely along the continuous paths of the printed tracks. In contrast, the interfaces between successive deposited layers constrain deformation in the build direction, leading to slightly lower thermal expansion values. Similar architecture-dependent anisotropy has been reported for additively manufactured ceramic scaffolds and infiltrated composite structures, where layer orientation governs both thermal and mechanical responses [23, 24].

A similar trend was observed during compression testing. Average compressive strengths of 511 MPa and 567 MPa were measured in the XY and Z directions, respectively. The approximately 11% increase in strength in the build direction indicates that the load-bearing capability of the interconnected ceramic skeleton depends on the orientation

of the printed architecture. The ceramic framework effectively transfers load from the ductile aluminum matrix, resulting in strengths substantially higher than those of conventional aluminum alloys. The relatively modest difference between the two testing directions further demonstrates that the infiltration process successfully produced a mechanically continuous structure while preserving the beneficial architectural features introduced during printing.

Overall, the results establish a direct relationship between the architecture generated by additive manufacturing, infiltration efficiency, and the resulting thermomechanical performance. The ability to design the ceramic framework prior to infiltration offers significant opportunities for tailoring the properties of AlN/Al composites for lightweight structural and thermal management applications. Furthermore, the proposed hybrid manufacturing approach enables the fabrication of multimaterial composites by combining different additively manufactured ceramic preforms that can be printed separately and subsequently infiltrated in a single processing step, thereby creating components with spatially tailored properties. Therefore, future work should focus on the fabrication and characterization of multimaterial ceramic–metal composites with locally optimized architectures, as well as on the evaluation of their thermal conductivity, elastic modulus, and long-term performance under thermal cycling.

Conclusion

An AlN/Al composite was successfully fabricated by combining pellet-based material extrusion of porous AlN preforms with pressure-assisted liquid aluminum infiltration. The debinding and sintering processes preserved the designed porous architecture, enabling efficient infiltration and the formation of a dense interpenetrating ceramic–metal structure. Microstructural analysis confirmed homogeneous aluminum distribution throughout the AlN framework and the formation of a well-defined AlN/Al interface. X-ray micro-computed tomography revealed a residual macroporosity of only 0.36%, while the overall porosity, determined by combining tomography and SEM analyses, was estimated to be approximately 0.68 vol.%. The final material consisted of 75.4 vol.% AlN and 24.6 vol.% Al. After thermal stabilization, the composite exhibited coefficients of thermal expansion of 11.6–12.9 × 10^{-6} K^{-1} and compressive strengths of 511 MPa and 567 MPa in the XY and Z directions, respectively, indicating only a minor influence of the printed architecture on the mechanical response. Overall, the results demonstrate that combining material extrusion with pressure-assisted liquid metal infiltration provides an effective route for producing architectured AlN/Al composites with low porosity and tailored thermomechanical properties, while establishing a clear processing–structure–property relationship for future design and optimization of ceramic–metal composites.

Declarations

Funding sources:

Funded by the EU NextGenerationEU through the Recovery and Resilience Plan for Slovakia under the project No. 09I03-03-V04-00715.

Author Contribution

S. N.: Writing – original draft, Visualization, Methodology, Investigation, Data curation, Conceptualization. L. V.: Review & editing, Supervision, Conceptualization. M. V.: Review & editing, Supervision, Investigation, E. N.: Review, Supervision, Conceptualization. A. O.: Methodology, Investigation, Data curation. L. K.: Methodology, Investigation. V. N. T.: Review & editing, methodology, Investigation. S. B. C.: Methodology, Investigation. P. O.: Methodology, Investigation.

Acknowledgement

The authors would like to thank Ing. Otto Bajana for conducting the compression tests and Ing. Tomáš Dvorák PhD. for his assistance with the metal infiltration process.

References

1. Koller C, Bauer W, Schober M et al (2023) Aluminium matrix composite materials reinforced by 3D-printed ceramic preforms. Materials 16:5473. https://doi.org/10.3390/ma16155473
2. Zhu C et al (2018) Additive manufacturing of complex 3D Al2O3 structures and infiltration with aluminum. J Eur Ceram Soc 38:3814–3823. https://doi.org/10.1016/j.jeurceramsoc.2018.04.037
3. Zhang Y, Liu D, Wang X et al (2025) Fabrication of SiC–aluminum composites via binder jetting and infiltration. J Compos Sci 9:111. https://doi.org/10.3390/jc9030111
4. Liu Z, Li Y, Shi Y (2019) 3D printing of porous ceramics for composite infiltration. Ceram Int 45:140–146. https://doi.org/10.1016/j.ceramint.2018.09.112
5. Cramer CL, Elliott AM, Kiggans JO, Haberl B, Anderson DC (2019) Processing of complex-shaped collimators made via binder jet additive manufacturing of BnC and pressureless melt infiltration of Al. Mater Des 180:107956. https://doi.org/10.1016/j.matdes.2019.107956
6. Gonzalez-Gutierrez A, Cano S, Schuschnigg S, Kukla C, Sapkota J, Holzer C (2017) Additive manufacturing of metallic and ceramic components by the material extrusion of highly-filled polymers: a review and future perspectives. Addit Manuf 18:110–127. https://doi.org/10.1016/j.addma.2017.09.013
7. Lewis JA (2006) Direct ink writing of 3D functional materials. Adv Funct Mater 16:2193–2204. https://doi.org/10.1002/adfm.200600434
8. Smay JE, Lewis JA, Cesarano J (2002) Colloidal inks for direct-write assembly. J Am Ceram Soc 85:2486–2494. https://doi.org/10.1111/j.1151-2916.2002.tb00468.x
9. Singh S, Singh R, Ramakrishna S (2017) Material issues in additive manufacturing: a review. J Manuf Process 25:185–200. https://doi.org/10.1016/j.jmapro.2016.11.006
10. Liu YQ, Cong HT, Wang W, Sun CH, Cheng HM (2009) AlN nanoparticle-reinforced nanocrystalline Al matrix composites: fabrication and mechanical properties. Mater Sci Eng A 505:151–156. https://doi.org/10.1016/j.msea.2008.11.031
11. Topic M et al (2010) Nanoscaled Al–AlN composites consolidated by equal channel angular pressing of partially nitrided Al powder. Mater Sci Eng A 527:2190–2195. https://doi.org/10.1016/j.msea.2009.11.020
12. Topic M et al (2011) Industrially fabricated in-situ Al–AlN metal matrix composites (Part B): mechanical, creep, and thermal properties. Mater Sci Eng A 528:1612–1618. https://doi.org/10.1016/j.msea.2010.11.034
13. Lee HM, Bharathi K, Kim DK (2004) Processing and characterization of aluminum nitride ceramics for high thermal conductivity. J Am Ceram Soc 87:198–203. https://doi.org/10.1111/j.1551-2916.2004.00198.x
14. Zhou Y et al (2014) High-thermal-conductivity AlN ceramics prepared from octyltrichlorosilane-modified AlN powder. Ceram Int 40:12413–12418. https://doi.org/10.1016/j.ceramint.2014.04.082
15. Zhou Y, Li G, Jia Z et al (2021) Additive manufacturing of aluminum nitride ceramics with high thermal conductivity. Open Ceram 7:100161. https://doi.org/10.1016/j.oceram.2021.100161
16. Zhang L, Gao S, Sun B et al (2006) Properties of AlN-based magnesium-matrix composites produced by pressureless infiltration. Mater Sci Forum 509:105–110. https://doi.org/10.4028/www.scientific.net/MSF.509.105

17. Yin S, Zhang Y, Liu X (2017) Thermal and mechanical properties of AlN reinforced aluminum composites. Mater Sci Eng A 699:1–8. https://doi.org/10.1016/j.msea.2017.05.036
18. Zhang H, Wang J, Liu L (2015) AlN particle-reinforced aluminum composites fabricated by infiltration. Compos Part B 71:1–7. https://doi.org/10.1016/j.compositesb.2014.11.012
19. Li J, Wu Y, Zhang X (2012) Pressureless infiltration of Al into AlN preforms. J MatSci 47:1234–1240. https://doi.org/10.1007/s10853-011-5932-4
20. Ray B, Oskolkov B, Liu C, Leblanc Z, Tian W (2023) FFF-based metal and ceramic additive manufacturing: production scale-up from a stream of variation analysis perspective. Manuf Lett 35:811–821. https://doi.org/10.1016/j.mfglet.2023.08.126
21. Seleznev M, Roy-Mayhew JD (2021) Bi-metal composite material for plastic injection molding tooling applications via fused filament fabrication process. J Additive Manuf 48:102375. 10.1016/j.addma.2021.102375
22. Ha SJ, Lee YK, Jeong KC et al (2024) Binder jetting and melt infiltration for ceramic–metal fuel fabrication. Ceram Int 50:48583–48591. 10.1016/j.ceramint.2024.09.206
23. Meng X et al (2025) Anisotropy and damage tolerance in zigzag-structured Al/Al2O3 composites fabricated via 3D printing and pressure infiltration. Ceram Int 51(21). 10.1016/j.ceramint.2025.05.121
24. Martin JH, Yahata BD, Hundley JM et al (2021) Fabrication of 3D metal–ceramic (Al–AlN) architectures using laser powder bed fusion. Addit Manuf 37:101698. https://doi.org/10.1016/j.addma.2020.101698

Figures

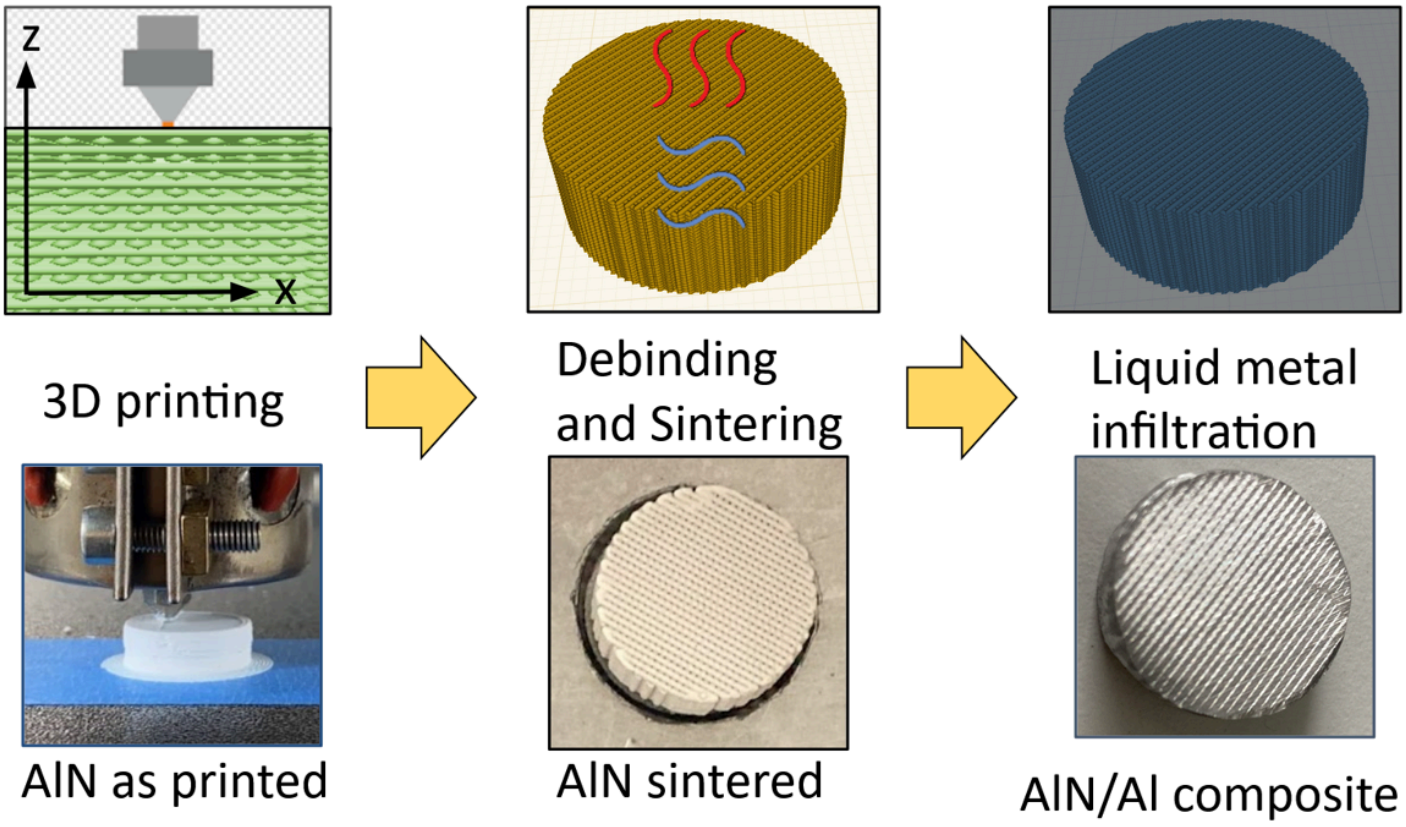


Figure 1

Schematic of the preparation route of the AlN/Al composite

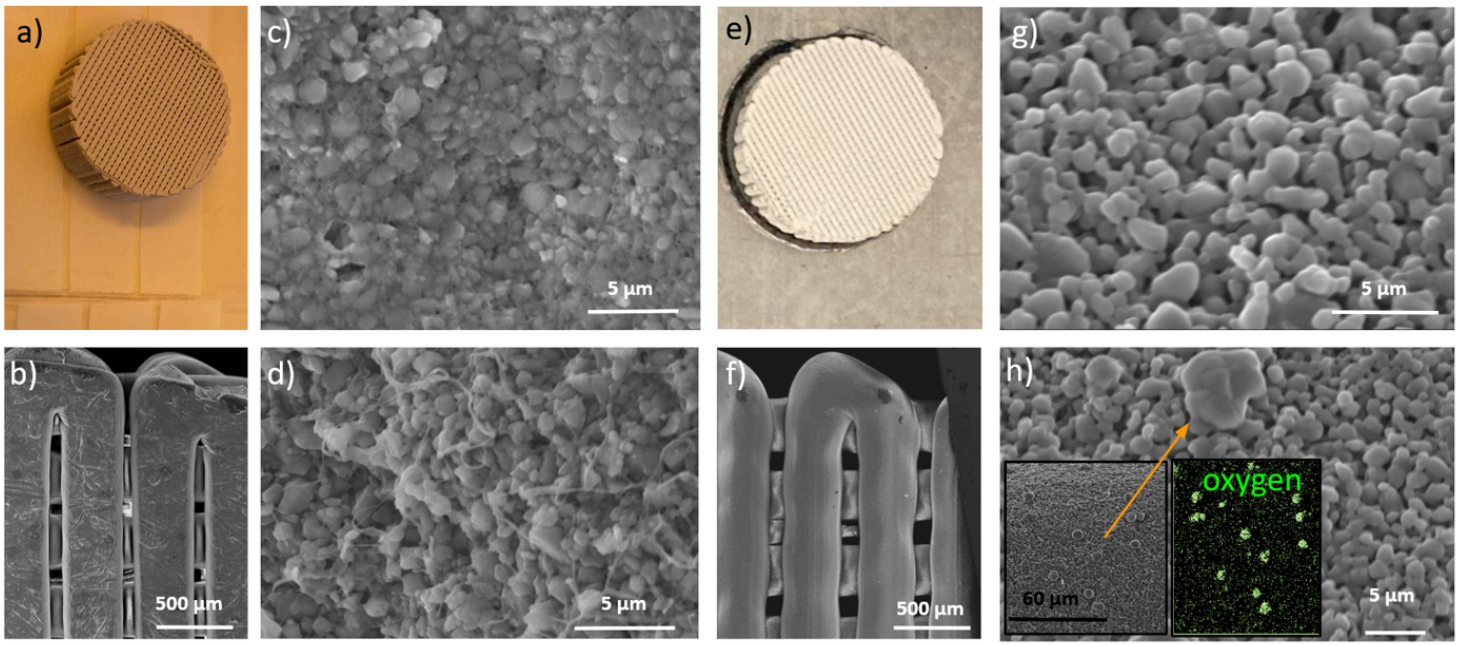


Figure 2

Macro and microstructure of the 3D printed preform surface: (a) as-printed sample; (b) line infill macrostructure; (c) surface microstructure of the as-printed AlN; (d) detail of the AlN particles with the visible bonding material on a fractured area; (e) sample after sintering; (f) line infill macrostructure after sintering; (g) surface structure showing AlN sintered particles; (h) spherical particles on the surface including oxygen EDS map.

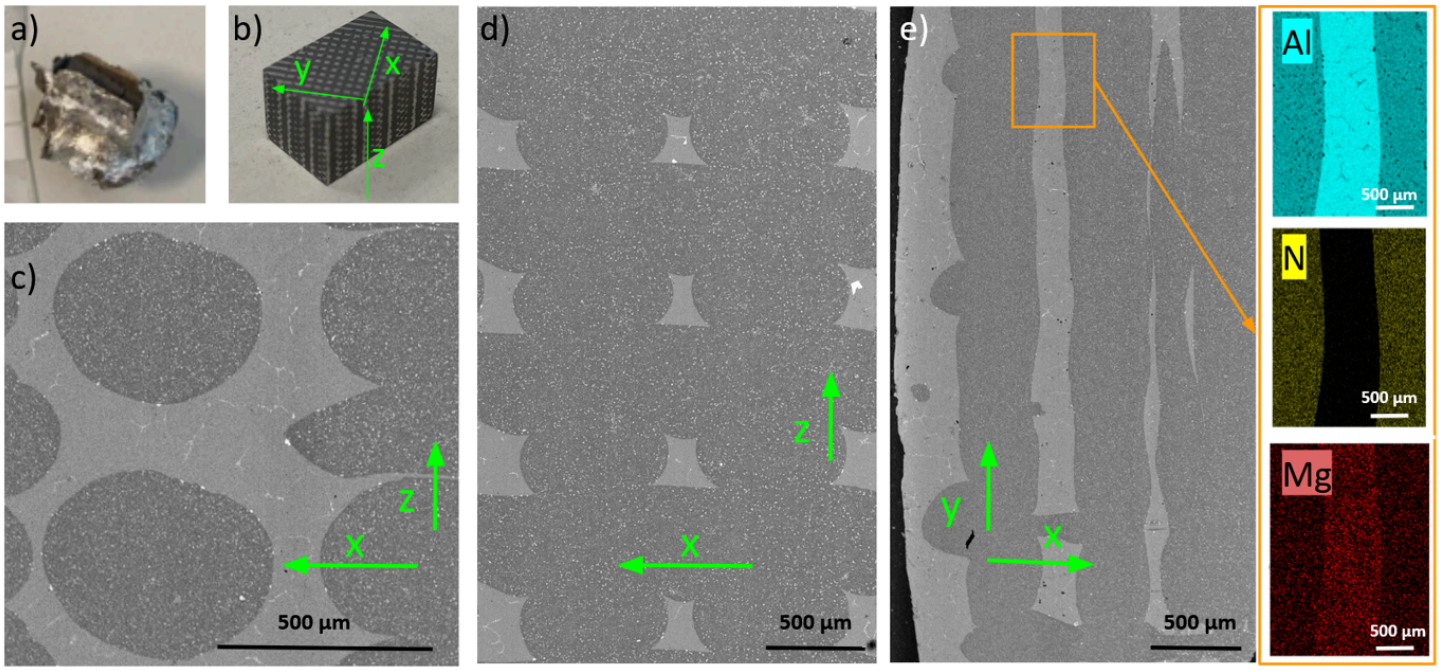


Figure 3

AlN/Al composite: (a) after the infiltration process; (b) cut and ground sample showing the X, Y, and Z build directions of the AlN structure; (c) microstructure perpendicular to the Y direction, showing the shape and size of individual ceramic lines; (d) microstructure perpendicular to the Y direction, showing the cross-sections of the Y- and X-oriented ceramic lines with infiltrated Al; (e) microstructure perpendicular to the Z direction with EDS elemental maps of Al, N, and Mg.

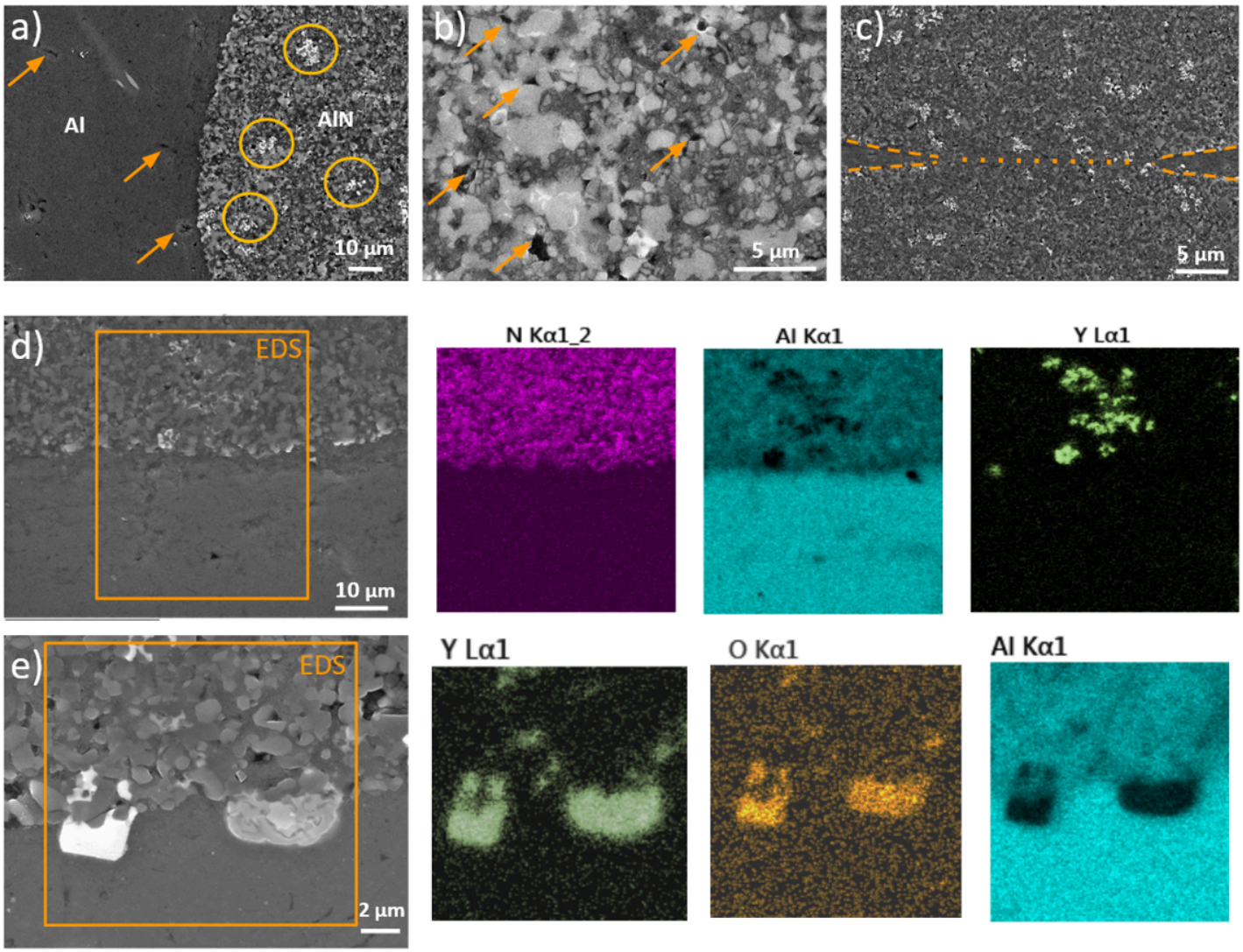


Figure 4

Microstructural investigation of the AlN/Al interface and the AlN ceramic phase showing: (a) the AlN/Al interface, with arrows indicating microporosity and circles highlighting high-contrast particles in the ceramic region; (b) the AlN ceramic microstructure showing microporosity; (c) the interface between two adjacent 3D-printed AlN lines; (d) a representative AlN/Al interface with corresponding EDS elemental maps; and (e) a higher-magnification view of the interface containing yttrium-rich oxide particles with corresponding EDS elemental maps.

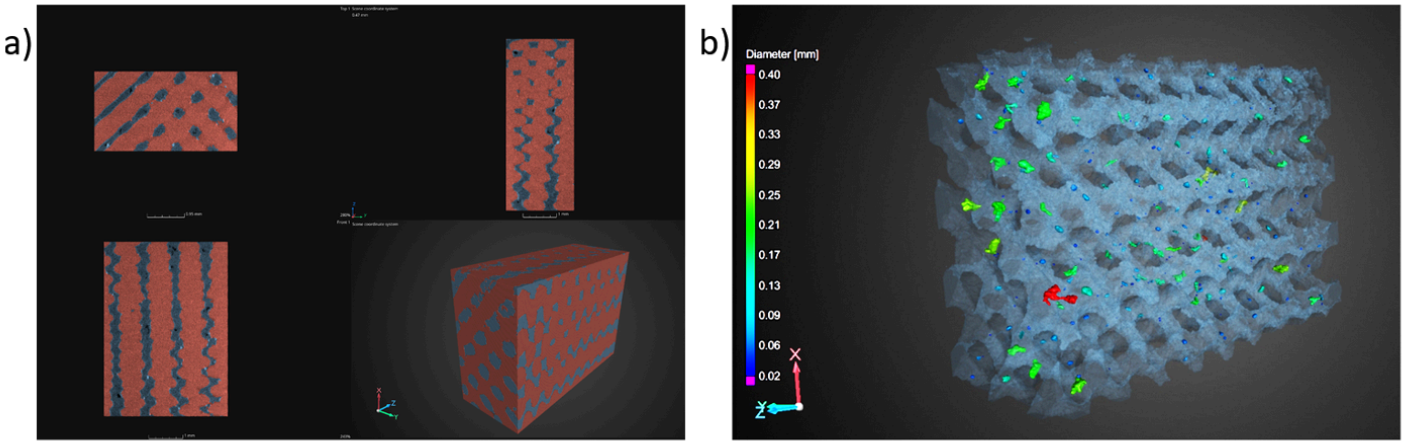


Figure 5

Volume fractions of the constituent phases (a) determined by microtomography and porosity measurements (b) of the aluminum alloy component

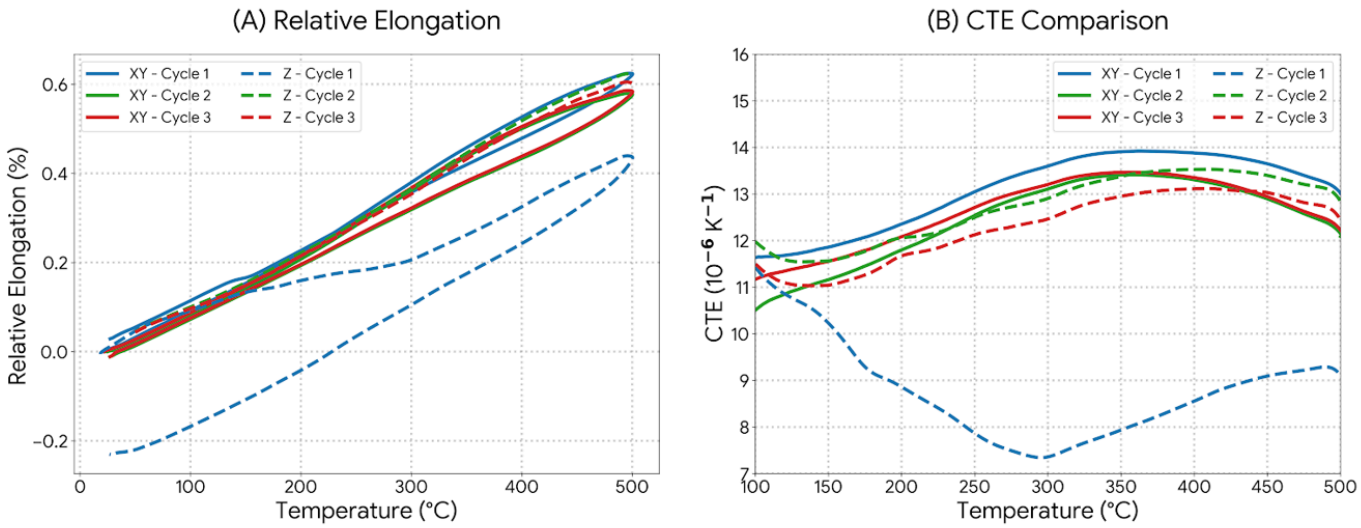


Figure 6

Thermomechanical analysis of the AlN/Al composite: (A) Temperature dependence of relative elongation for three heating-cooling cycles, showing structural stabilization and shrinkage in the Z-axis. (B) Instantaneous CTE values from 100 °C to 500 °C. Solid lines represent the XY plane (printing plane), and dashed lines represent the Z-axis (build direction). Colors indicate the sequence of cycles: Cycle 1 (blue), Cycle 2 (green), and Cycle 3 (red).